International Journal of Modern Manufacturing Technologies
ISSN 2067–3604, Vol. XIV, No. 1 / 2022
https://doi.org/10.54684/ijmmt.2022.14.1.64

INVESTIGATION ON EFFECT OF PULSED CURRENT MICRO PLASMA ARC WELD PARAMETERS ON UNS S32750 SUPER DUPLEX STAINLESS STEEL SHEETS

Sasidhar Gurugubelli[1], V.V.S. Kesava Rao[2]

[1]Department of Mechanical, Andhra University and faculty of Engineering, Department of Mechanical, GMR Institute of Technology, Rajam, India, 532127
[2]Faculty of Engineering, Department of Mechanical, Andhra University, Visakhapatnam, India

Corresponding author: Sasidhar Gurugubelli, sasidhar.g@gmrit.edu.in

Abstract: In this paper, a 0.33mm thick UNS S32750 super duplex stainless steel sheet is butt welded with welding with a micro-plasma arc. Peak current, base current, pulse width, and pulse rate are regarded welding input factors, whereas the tensile strength and hardness of the welded joint are known as output parameters. 31 distinct combinations of tests are carried out by integrating the response surface method (RSM) with central composite design (CCD) and taking into account four factors and five levels of weld process parameters. The main plots are used to visualize the variance in output responses as a function of weld input parameters. MINITAB software is used to establish mathematical models that take into account linear functions. At a 95% confidence level, ANOVA is used to compare two variables. The dominant parameter is identified using contour plots, and the optimum combination of welding parameters is determined using surface plots. Various welding parameters and their effect on stainless duplex steels have been comprehensively explored in this study.

Key words: Micro Plasma Arc Welding, UNS S32750 Super Duplex Stainless Steel, Response Surface Method.

1. INTRODUCTION

Duplex stainless steels (DSS) have an important passive advantage over other stainless steels due to their strong toughness and low Ni content. Furthermore, due to its high resistance to pitting corrosion, design engineers prefer DSS to austenitic stainless steels as constructing and enclosing assemblies where attack by chloride is a major issue. For DSS to work properly, the microstructure must have an austenite/delta-ferrite diffusion with the fewest secondary phases possible. For DSS to work properly, the microstructure must have an austenite (γ)/ delta-ferrite (δ) diffusion with the fewest secondary phases possible [1]. Any kind of heating of DSS above 300ºC, for example fusion welding, can cause the microstructure to deteriorate [2-4]. The weld quality and cooling rate are the major determinant of as-welded DSS metallurgy. Rapid cooling retains more ferrite and increases the likelihood of nitride precipitation, in contrast to high cooling rates hold more ferrite, which increases the likelihood of nitride precipitation during welding [5,6]. Spinodal decomposition of Cr-rich-ferrite (αı) is more likely when cooling rates are slow and welding time is long, namely embrittlement, and Precipitation of intermetallic elements, as an example sigma (σ) and chi (χ) [7]. In order to achieve moderate cooling speeds, heat intake must be kept within the higher and lower bounds, and inter-pass temperatures should be held at a minimum (180–200ºC) during conventional multi-pass Welding by fusion. Controlling some welding parameters with a poor accuracy during standard multi-pass welding procedures requires additional man-hours in manufacturing and fabrication [8].

Plasma arc welding (PAW), electron beam welding (EBW), laser beam welding (LBW) and hybrid Laser arc welding (HLAW) may all be used to produce single pass DSS weldments. These welding methods, on the other hand, are only suitable for joints with a very limited gap or none at all, it is hard to put the right amount of filler metal, which contains a lot of Ni, to the steel weld to be able to get appropriate γ in δ matrix [9,10]. In addition to their extremely low heat capacity, keyhole welding that is fully or partially autogenous may result in an accumulation of δ-ferrite erecting in as welded DSS that prompts worsening of the toughness and resistance to corrosion of the material [11,12]. Consequently, post-weld procedures such as solutionizing are usually required for DSS PAW, LBW, HLAW, and EBW in order to obtain a weld metal microstructure free of secondary phases and with adequate phase balance [13].

The properties of DSS are relying upon the austenite-ferrite phase ratio, which is considered to be nearly

1:1 to obtain adequate properties [14]. The heat-affected zone (HAZ) phase ratio aims to diverge from 1:1 after the welding thermal cycle. There must be some degree of austenite reformation in the DSS HAZ in order to stay away from the formation of damaging chromium-rich nitrides, which are most commonly found inside ferrite grains, to ensure good resistance and impact energy [15].

2. LITERATURE REVIEW

Earlier studies conducted by researchers using plasm arc welding on duplex stainless steels are presented in this section.

Flux Cored Arc Welding (FCAW) parameters optimized in accordance with the Taguchi specifications to weld 2205 DSS ferrite material [16]. Analysis was done on regression model progress and FCAW 2205 duplex stainless steel process parameter optimization [17]. Yurtisik *et al*., examined the characterization of hybrid plasma arc welded duplex stainless-steel weldments [18]. Genetic algorithms (GA) with invasive weed optimization (IWO) algorithms were used to examine the mechanical and microstructural characterization of 2205 duplex stainless steel formed via gas metal arc and hybrid plasma welding. For bead width and bead height, additional non-linear regression calculations have been made. According to the optimization results, the IWO algorithm outperforms the GA in terms of bend bead width and height [19, 20].

Welding of 2205 duplex stainless steel plates using keyhole plasma arc was examined using three-dimensional modelling of thermal finite elements [21]. To test different laser powers (1500, 2000, and 2500W) and welding rates (60, 40, and 20 mm/s), a YAG fibre laser machine was used to weld a 304L stainless steel plate that was 3mm thick at a fixed defocusing distance of -2mm. It analyses the effect of welding speed and welding current on the quality of welded joints. Performance characteristics such as bead geometry, microstructure, hardness, ferrite measurement, and tensile tests are considered [22]. Microstructure, mechanical properties and degradation behaviour of UNS S32750 super duplex stainless steel components with a thickness of 5.5 mm were investigated. Using the shielded metal arc welding procedure, the experiment used ER2594 and ER2595 electrodes to build butt joints [23]. With two different heat inputs, 0.54 and 1.10kJ/mm, investigating the effects of heating duplex stainless steel shielded metal arc junctions on their microstructure and corrosion behaviour [24]. The underwater arc welding method was used to examine the impact of heat contribution on the mechanical properties and microstructures of API 5L-X65 steel [25].

MPAW, or micro plasma arc welding with pulsed current, is used to connect 0.33 mm thick sheets of UNS S32750 super duplex stainless steel in this study. This study was conducted to determine how welding parameters including peak current, base current, pulse width, and pulse rate affect the fusion zone tensile strength and hardness of the welded joint.

3. MATERIALS AND METHODS

An autogenous square butt joint is used to join stainless steel sheets UNS S32750 with dimensions of 100x240x0.33mm. Chemical and mechanical properties of UNS S32750 super duplex stainless steel are shown in Tables 1 and 2.

Table 1. Chemical composition of UNS S32750 (weight %) [2,3,23]

Ni	Cr	Mn	Mo	Fe
6.69	25.04	1.00	3.25	64.02

Table 2. Mechanical properties of UNS S32750 [2,3,23]

Elongation (%)	Ultimate Tensile Strength (MPa)	Vickers Hardness (VHN)
21.8	923.160	259.7

Atmospheric absorption of oxygen and nitrogen are prevented during welding by using highly pure (99.99 per cent) argon as a shielding and trailing gas. Table 3 lists the welding conditions under which the welding was performed.

Table 3. Welding Conditions

Power source	Secheron Micro Plasma Arc Machine (Model: PLASMAFIX 50E)
Polarity	DCEN
Mode of operation	Pulse mode
Electrode	2% thoriated tungsten electrode
Electrode Diameter	1 mm
Plasma gas	Argon & Hydrogen
Plasma gas flow rate	6 Lpm
Shielding gas	Argon
Shielding gas flow rate	0.6 Lpm
Purging gas	Argon
Purging gas flow rate	0.6 Lpm
Copper Nozzle diameter	1mm
Nozzle to plate distance	1mm
Welding speed	240 mm/min
Torch Position	Vertical
Operation type	Automatic

MPAW weld consistency characteristics with pulsed current process are persuaded by operation parameters including weld speed and shielding gas pass as well as base current and peak current, pulse width and pulse frequency.

Pulsed Current According to MPAW research, the most important weld quality parameters to consider are peak current, base current, pulse width and pulse rate [26, 27]. Trial experiments and material thickness are used to determine the welding parameter ranges. As a result, the limits of the base current, peak current, pulse rate, and pulse width have been determined and these results can be found in Table 4.

Table 4. Process parameters and their limits

	Levels					
Input Factor	Units	-2	-1	0	+1	+2
Peak Current	A	18	19	20	21	22
Base Current	A	8	9	10	11	12
Pulse rate	Pulses /s	20	30	40	50	60
Pulse width	%	30	40	50	60	70

3.1 Determination of Fusion Zone Grain Size

Three metallurgical test specimens are taken from every joint, but the corners of the welded length are not included. Visually, as well as by dye penetrant and X-ray checks, the length of the weld that is faulty has been discovered and Bakelite is used to mount it. The ASTM E 3-1 norm is followed for sample preparation and mounting. The samples transverse faces are surface ground with a 120-grit size belt on a belt grinder, then polished using emery paper of grades 1/0 (245 mesh size), 2/0 (425 mesh size), and 3/0 (515 mesh size) in that order. A disc polishing system is used to polish the specimens further with aluminium oxide, diamond paste, and velvet fabric. To expose the microstructure, the polished specimens are etched with Carpenter Etchant solution.

The weld zone microstructure and grain size are exposed by varying the etching period. Figures 1, 2 and 3 show a micrograph of the parent metal, fusion zone (FZ), and heat affected zone (HAZ) at 100X magnification.

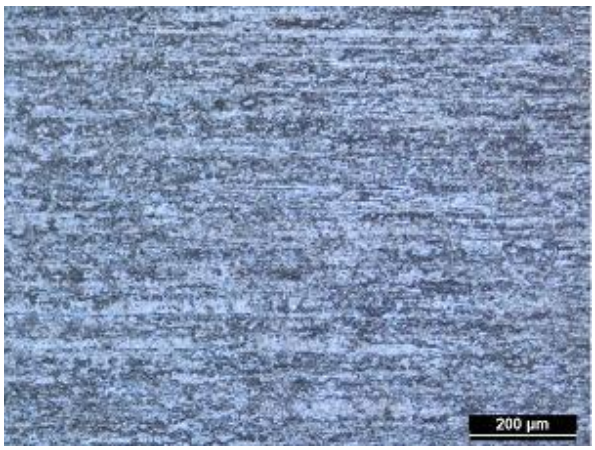

Fig. 1. Microstructure of parent metal

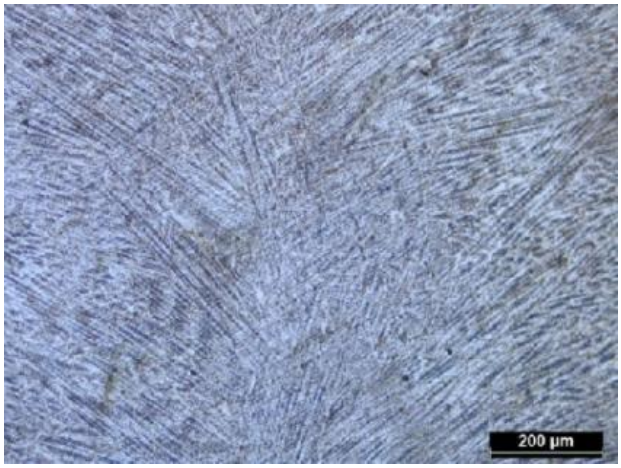

Fig. 2. Microstructure of fusion zone

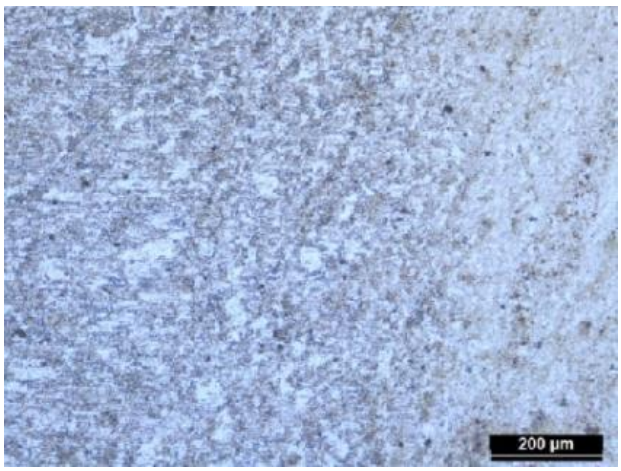

Fig. 3. Microstructure of heat affected zone

3.2 Measurement of Fusion Zone Hardness

Micro hardness testing machine by Vicker (Make: Banbros Engineering Pvt Ltd, India, Model: VHS 1000) the hardness of the fusion region may be determined, by applying a 0.5 kg weight on the fusion region of the welded samples and a dwell time of 10 seconds as per ASTM E384. For each sample, Table 5 gives the average values of three hardness readings.

3.3 Ultimate Tensile Strength (UTS) Measuring

Wire cut electro discharge machining was used to machine the weld in the transverse direction to prepare tensile weld specimens according to ASTM E8M-04 specifications (see Figure 4).

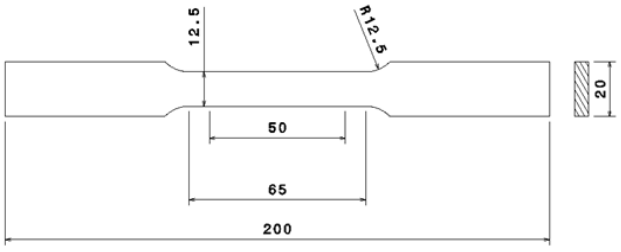

Fig. 4. Tensile specimen as per ASTM E8M-04

Tensile testing is conducted using a computer assisted universal testing machine with a 100 KN capacity and a short extensometer connected (Star Testing Systems, Sr.No.STS-522, Model No: 9036TD).
The ASTM specifications are followed, and the specimens are loaded at a constant rate of 1.5 KN/min, causing the tensile specimens to deform. The ultimate tensile strength of weld joints can be calculated using the stress strain curve (Figure 5), and the data in Table 5 shows the average of all the sample results.

Table 5. Experimental Results

Exp.No.	Welding Input Parameters				Experimental Output Values		Predicted Output Values	
	Peak Current (A)	Base Current (A)	Pulse Rate (Pulses/s)	Pulse Width (%)	Hardness (VHN)	Tensile Strength (MPa)	Hardness (VHN)	Tensile Strength (MPa)
1	19	9	30	40	251.2	846.52	250.8	846.891
2	21	9	30	40	248.2	860.20	249.2	858.820
3	19	11	30	40	246.8	854.53	247.2	851.137
4	21	11	30	40	246.8	850.82	246.9	850.736
5	19	9	50	40	250.6	860.40	250.6	860.080
6	21	9	50	40	252.2	868.28	252.5	866.400
7	19	11	50	40	252.4	862.34	252.1	860.521
8	21	11	50	40	254.8	854.62	255.3	854.510
9	19	9	30	60	253.8	850.42	254.6	848.839
10	21	9	30	60	252.8	852.62	252.3	857.123
11	19	11	30	60	251.6	846.46	250.5	851.025
12	21	11	30	60	248.2	848.35	249.5	846.979
13	19	9	50	60	250.4	838.86	249.5	841.628
14	21	9	50	60	249.6	842.60	250.5	844.302
15	19	11	50	60	250.2	840.32	250.5	840.009
16	21	11	50	60	253.2	828.04	252.8	830.353
17	18	10	40	50	242.2	838.28	243.1	838.637
18	22	10	40	50	245.2	842.26	243.9	840.910
19	20	8	40	50	248.2	848.42	247.9	846.825
20	20	12	40	50	246.8	836.52	246.7	837.122
21	20	10	20	50	254.2	858.68	253.7	858.362
22	20	10	60	50	256.8	855.60	256.9	854.925
23	20	10	40	30	257.4	870.25	256.9	875.053
24	20	10	40	70	258.2	858.64	258.3	852.843
25	20	10	40	50	254.6	853.29	253.0	853.223
26	20	10	40	50	252.4	854.53	253.0	853.223
27	20	10	40	50	252.1	853.24	253.0	853.223
28	20	10	40	50	253.8	852.68	253.0	853.223
29	20	10	40	50	252.2	852.24	253.0	853.223
30	20	10	40	50	253.8	852.26	253.0	853.223
31	20	10	40	50	252.3	854.32	253.0	853.223

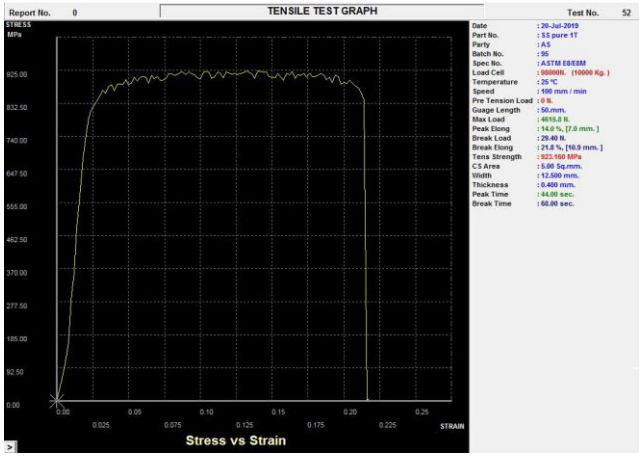

Fig. 5. Stress stain curve (parent metal)

The failure of tensile specimens is studied using scanning electron microscopy (SEM). All welding conditions produce ductile dimples in the interface/fusion zone of a specimen, as seen in Figures 6 and 7.

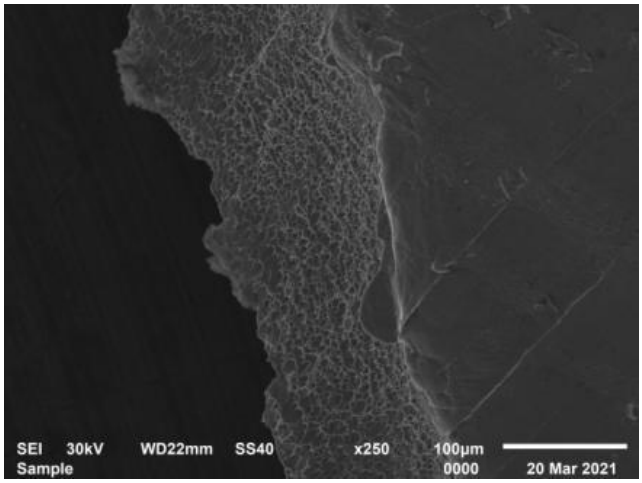

Fig. 6. SEM image at failure section

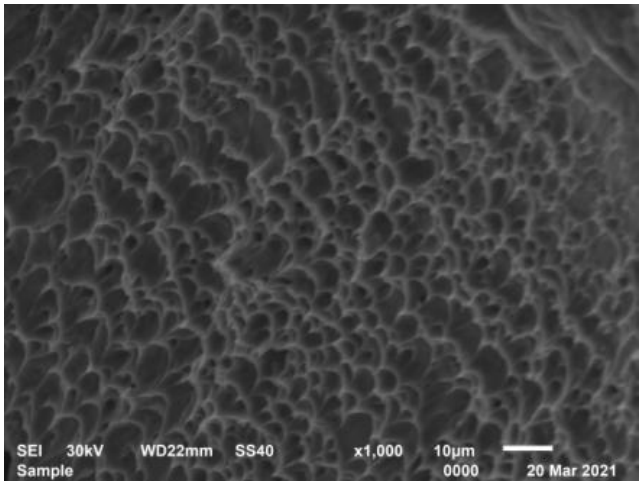

Fig. 7. SEM image indicating dimples at failure zone

To prevent systemic errors infiltrating the device, the experiments were carried out at random according to the design matrix.

4. RESULTS AND DISCUSSION

Statistical analysis is carried out sing MINITAB software and the details are presented.

4.1 Mathematical Modelling

A second order polynomial of the independent variables is used to used to establish a connection between the response and the independent variables. If a nonlinear function of the variables that are not dependent appropriately simulates the response, the estimating function in the second order regression is

$$Y = b_o + \sum b_i x_i + \sum b_{ii} x_i^2 + \sum b_{ij} x_i x_j + \in \quad (1)$$

where b_o, b_i are the polynomial coefficients and $\in$ denotes noise.

Empirical models are created using MINTAB software and the nonlinear model.

$$\text{Hardness} = 253.029 + 0.200X_1 - 0.317X_2 + 0.800X_3 + 0.350X_4 - 2.386X_1^2 - 1.436X_2^2 + 0.564X_3^2 + 1.139X_4^2 + 0.850X_1X_3 + 1.275X_2X_3 - 1.250X_3X_4 \quad (2)$$

$$\text{Tensile Strength} = 853.223 + 0.568X_1 - 2.426X_2 - 0.859X_3 - 5.553X_4 - 3.362X_1^2 - 2.812X_2^2 + 2.681X_4^2 - 3.083X_1X_2 - 5.100X_3X_4 \quad (3)$$

X_1, X_2, X_3 and X_4 represent the compiled attributes of peak current, base current, pulse rate and pulse width.

4.2 Analysis of Variance (ANOVA)

The ANOVA is used to determine if the built models are adequate. According to this technique, the model is deemed to be adequate within the confidence limit if the measured F_{ratio} of the model is smaller than the predefined F_{ratio} value (2.56) at the intended level of confidence of 95 %. Table 6 depicts the results of the ANOVA tests for hardness and tensile strength, for which the mathematical models created are deemed appropriate at a 95% confidence level.

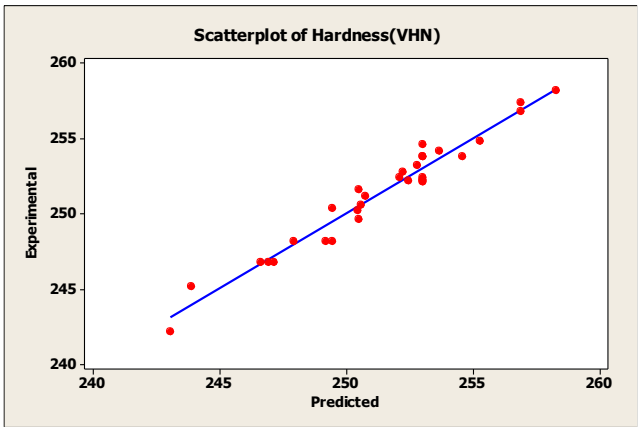

Fig. 8. Scatter plot for Hardness

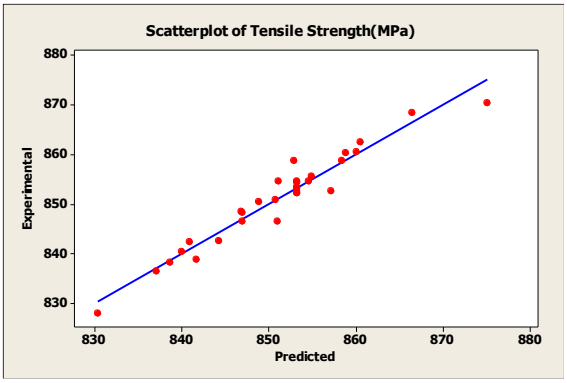

Fig. 9. Scatter plot for Tensile strength

Table 6 depicts the results of the ANOVA tests for hardness and tensile strength, for which the mathematical models created are deemed appropriate at a 95% confidence level.

In the following models, the coefficient of determination 'R^{2}' comes to around 0.957. To explain how similar the real (experimental) and expected values are, scatter plots are drawn as shown in Figures 8 and 9.

Table 6. ANOVA Table

Analysis of Variance for Hardness						
Source	DF	Seq. SS	Adj. SS	Adj. MS	F	P
Regression	14	375.114	375.114	26.794	25.73	0.000
Linear	4	21.667	21.667	5.417	5.20	0.007
Square	4	288.297	288.297	72.074	69.22	0.000
Interaction	6	65.150	65.150	10.858	10.43	0.000
Residual Error	16	16.661	16.661	1.041		
Lack-of-Fit	10	10.527	10.527	1.053	1.03	0.509
Pure Error	6	6.134	6.134	1.022		
Total	30	391.775				
Analysis of Variance for Tensile strength						
Source	DF	Seq. SS	Adj. SS	Adj. MS	F	P
Regression	14	2388.69	2388.686	170.620	18.30	0.000
Linear	4	906.63	906.626	226.657	24.31	0.000
Square	4	850.39	850.391	212.598	22.80	0.000
Interaction	6	631.67	631.669	105.278	11.2	0.000
Residual Error	16	149.21	149.206	9.325		
Lack-of-Fit	10	144.10	144.101	14.410	16.94	0.001
Pure Error	6	5.10	5.105	0.851		
Total	30	2537.89				

where DF=Degree of Freedom, SS=Sum of Squares, MS=Mean Square, F=Fisher's Ratio

4.3 Main effect plots

Main effect plots as shown in Figure 10 and 11 are drawn to understand the variation of each individual welding parameter on output responses namely hardness and tensile strength.

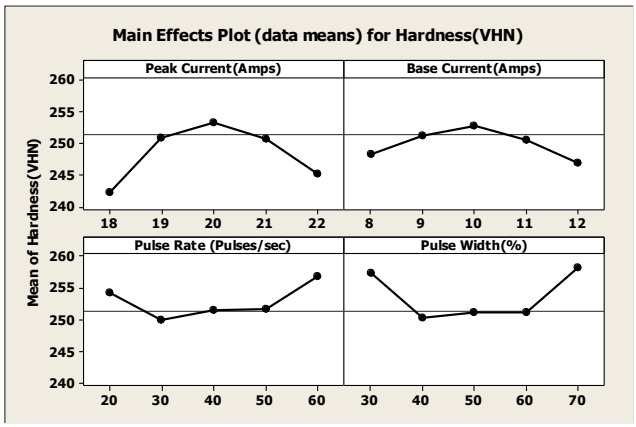

Fig. 10. Main effect plot for Hardness

Hardness and tensile strength increase as the peak current rises from 18 to 20 Amps, owing to proper fusion of the base metal as the heat input rises. However, when the peak current crosses 20 Amps, the hardness and tensile strength decrease because of over melting of base metal. Base current helps in maintain the arc during pulsed current mode of welding. Base current follows the trend of peak current. From 8 Amps to 10 Amps, hardness and tensile strength increase, then decrease.

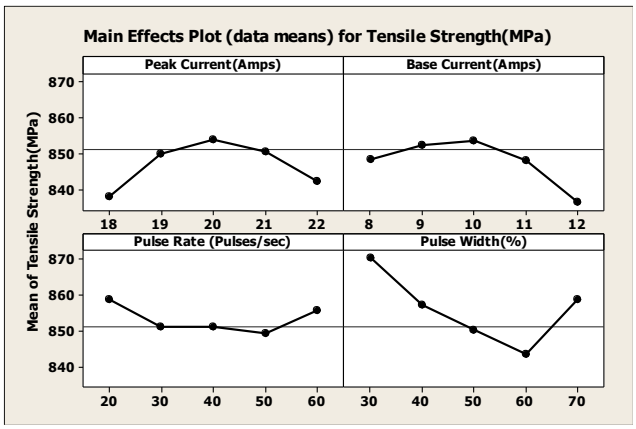

Fig. 11. Main effect plot for Tensile strength

Pulse rate plays an important role in maintain the quality of the weld joint. Pulse rate is almost stable between 40 to 50 pulse/second. Low pulse rate leads to faster cooling rate and coarse grain formation, whereas at higher pulse rate slower cooling rate and formation of fine grains. Because of grain refinement and finer grain formation hardness and tensile strength improves.

Pulse width indicates the time duration for cooling the weld metal. Higher the pulse width lower faster cooling rate and vice versa. Hardness is almost stable between 50 to 60 %, whereas decrease in tensile strength is observed between 30 to 60 % pulse width. They could be caused by martensite production at high temperatures during welding. When high-temperature austenite is quickly cooled below a critical temperature, martensite forms. It has a high strength-to-weight ratio, low fracture resistance, and low ductility.

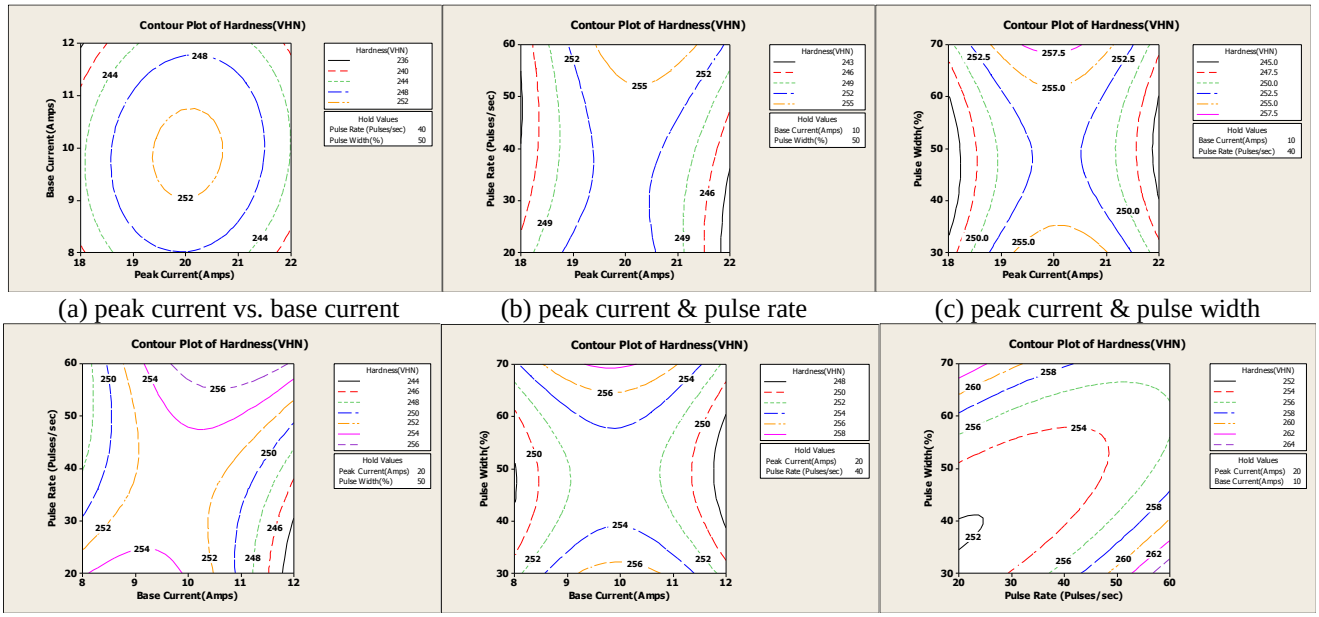

(a) peak current vs. base current (b) peak current & pulse rate (c) peak current & pulse width

(d) base current & pulse rate (e) base current & pulse width (f) pulse rate & pulse width

Fig. 12. Contour plots for Hardness

In a procedure known as tempering, it can be maintained at an intermediate temperature for a period of time to diminish strength while greatly improving toughness and ductility. Both alloy and stainless steels can produce martensite.

4.4 Contours Plots

Contours plots are drawn to identify the dominating welding parameter. Generally, contours are drawn between to parameters.

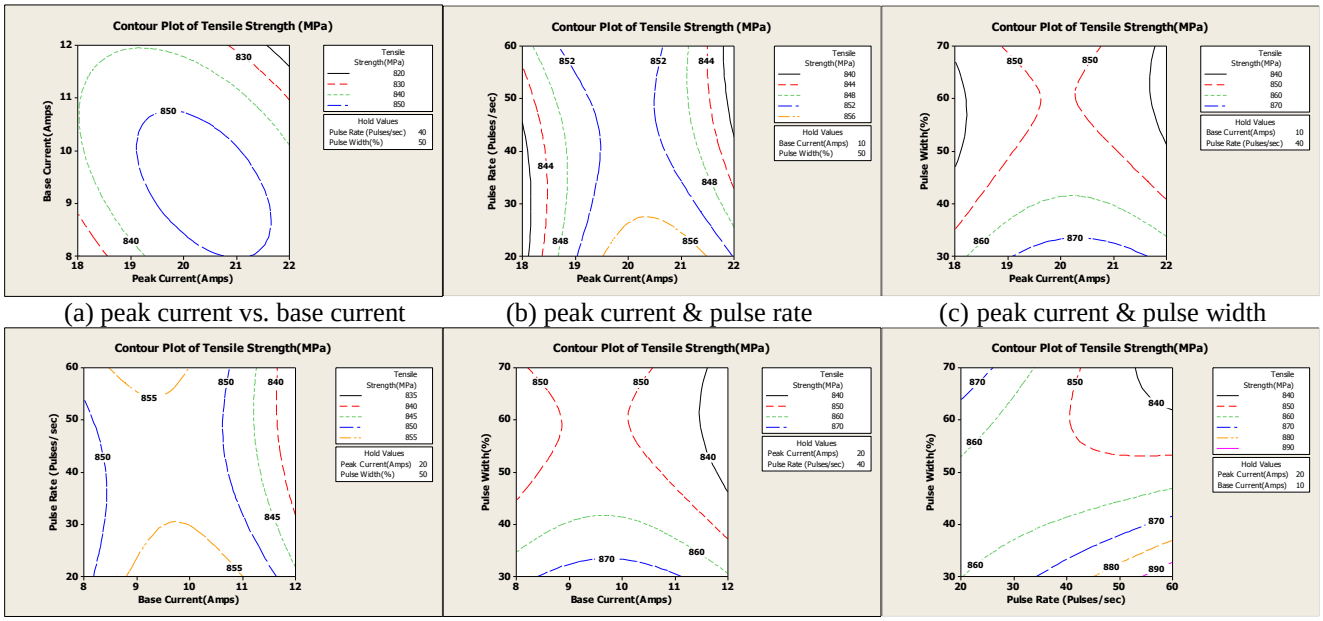

(a) peak current vs. base current (b) peak current & pulse rate (c) peak current & pulse width

(d) base current & pulse rate (e) base current & pulse width (f) pulse rate & pulse width

Fig. 13. Contour plots for Tensile strength

If the contour is circle in shape, it represents that both the parameters are having equal influence on the output. If the contour is elliptical in shape, the parameter which is towards major axis is more dominant than the other. If the contours are diverging, it represents negligible or minimum effect on output response. Figure 12 and 13 represents the contour plots for hardness and tensile strength.

Peak current and base current have nearly equal effects on hardness, as seen in Figure 12(a). From Figure 12(b), 12(c), 12(d), 12(e), as the contours are diverting away, both have minimum influence on hardness. From Figure 12(f), contours are diverging towards pulse rate, hence pulse rate is more dominating than pulse width.

Peak current has the upper hand over base current, as seen in Figure 13(a). From Figure 13(b), 13(c), 13(d), 13(e), 13(f) as the contours are diverting away, both have minimum influence on tensile strength.

4.5 Surface plots

Surface plots are used to identify the optimal values based on the curvature of the curve. For maximum value we should consider apex of the curve surface, whereas for minimum value we should consider nadir. Figure 14 and 15 represents the surface plots for hardness and tensile strength.

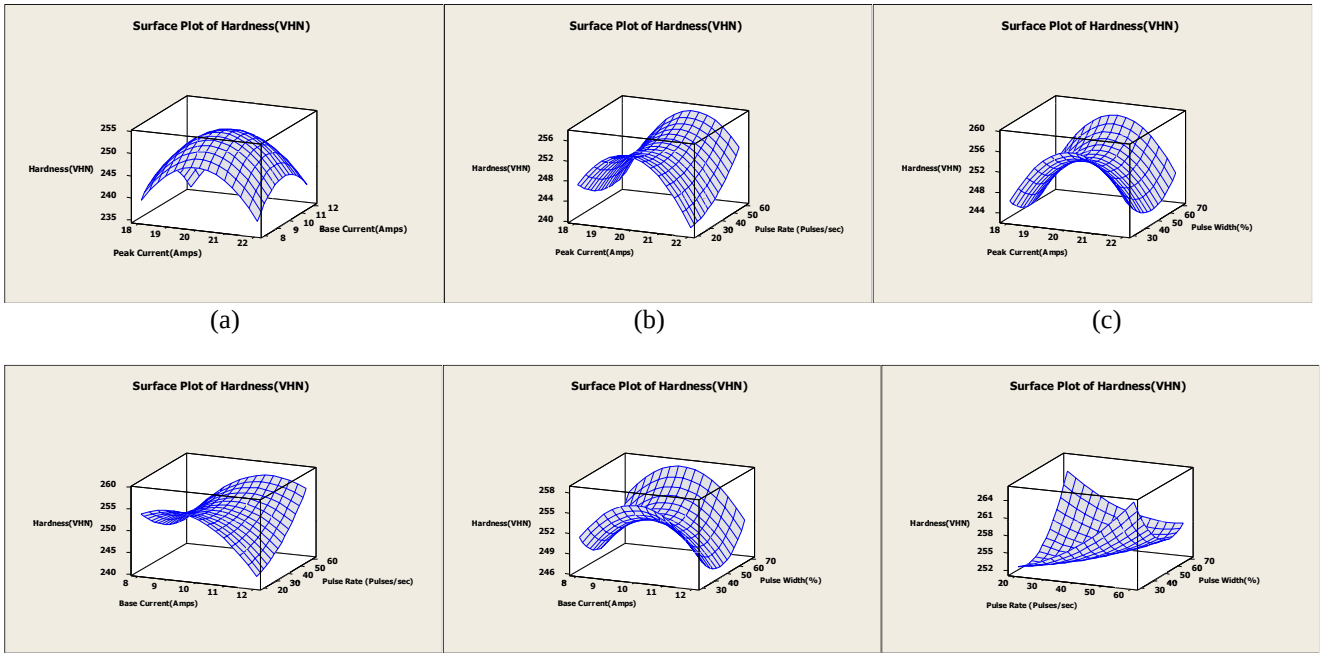

(a) (b) (c)

(d) (e) (f)

Fig. 14. Surface plots for Hardness vs. a) peak current & base current, b) peak current & pulse rate, c) peak current & pulse width, d) base current & pulse rate, e) base current & pulse width, f) pulse rate & pulse width

As depicted in Figure 14(a), maximum hardness can be achieved by using a peak current of 20 amps and a baseline current of 11 amps. Figure 14(b) shows how to use 20 amps peak current and a pulse rate with 60 pulses per second to achieve maximum hardness. 20 amps peak current and 30% pulse width can produce a 30 percent increase in maximum hardness (Figure 14(c)). Maximum hardness can be achieved with 11 Amps of base current and a pulse rate with 60 pulses/second, as shown in Figure 14(d).

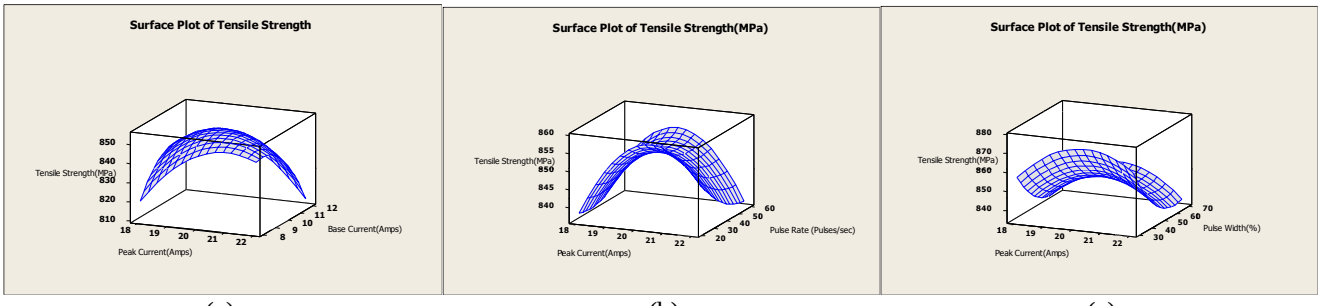

(a) (b) (c)

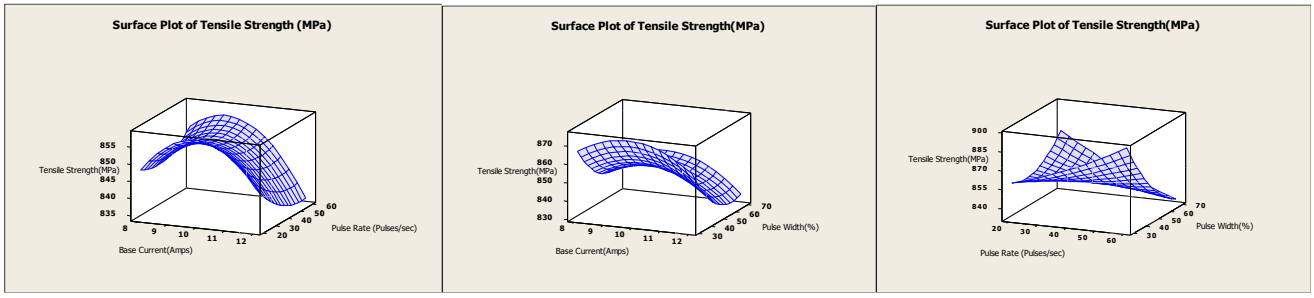

(d) (e) (f)

Fig. 15. Surface plots for Tensile strength vs. a) peak current & base current, b) peak current & pulse rate, c) peak current & pulse width, d) base current & pulse rate, e) base current & pulse width, f) pulse rate & pulse width

A maximum hardness of 30 percent can be achieved with 11 Amps of base current and of 30 percent pulse width (see Figure 14(e)). Using the pulse rate and pulse width shown in Figure 14(f), a maximum hardness of 60 pulses per second and 30 percent can be achieved.

Figure 15(a) depicts the maximum tensile strength at a 20-amp peak and an 11-amp base current. 20 amps peak current and a pulse rate with 60 pulses per second are required to achieve maximum hardness, as shown in Figure 15(b). Using 20 amps peak current and 30% pulse width, the tensile strength can be increased by 30%. Maximum tensile strength can be achieved by using a base current of 11Amps as well as a pulse rate with 60 pulses/second, as shown in Figure 15(d). Using the 11 amps base current and the 30% pulse width, the maximum tensile strength can be increased by 30% (see Figure 15(e)). A pulse rate with 60 pulses per second combined with a 30 percent pulse width results in the maximum tensile strength shown in Figure 15(f).

5. OPTIMIZATION

According to Figure 16, 21.75 Amps of peak current, 8.20 Amps of base current, a pulse rate with 60 pulses/second, and 30% pulse width were found to be the optimal response surface method solution for maximum hardness and tensile strength.

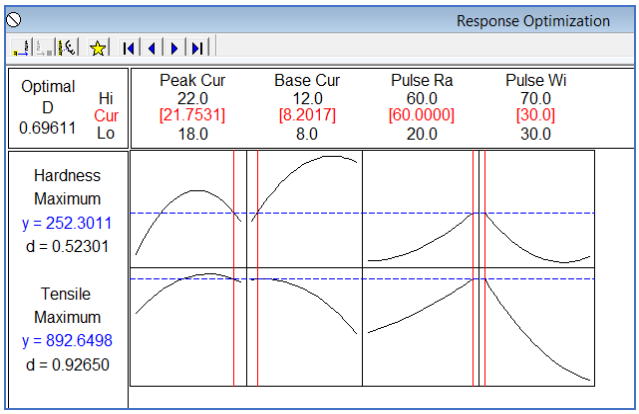

Fig: 16 Surface optimizer plot

6. CONCLUSION

Based on the results of the experiments, the following conclusions have been drawn.

i) The coefficient of determination for hardness and tensile strength is about 0.957, and analysis of variance is conducted at a 95% confidence level. UNS S32750 super duplex stainless steel sheet of 0.33mm thick was successfully welded using pulsed current MPAW process.

ii) Empirical mathematical models are developed considering second order polynomial equation as the welding involves curvature.

iii) At a 95% confidence level, an analysis of variance is performed and coefficient of determination for hardness and tensile strength is about 0.957.

iv) Peak current and base current rise up to a certain limit and then begin to decrease, as seen in the main effect plots, as a result of the base metal being overheated. Hardness and tensile strength are stable between pulse rate of 40 and 50 pulses/second. Hardness and tensile strength decreased with pulse width up to 60 % Pulse width decreased with and thereafter slightly improved.

v) Peak current is the most dominant welding parameter, accompanied by pulse rate, base current, and pulse duration, according to the contour plots.

vi) Maximum tensile strength and hardness in accordance with the surface plots, obtaining values at a maximum of 20 amps, 11 amps of base current, pulse rate with 60 pulses per second, and 30% pulse width.

vii) Maximum 252.30 VHN and 892.649MPa tensile strength were obtained from the response optimizer at 21.75 Amps of peak current, 8.20Amps of base current, pulse rate with 60 pulses/second, and 30% pulse width.

7. REFERENCES

1. Sasidhar Gurugubelli and Kesava Rao, (2021) *Inclusive Review on Welding of Duplex Stainless*

Steels, Proceedings of CAMSE 2020, Advances in Mechanical Engineering, Gaurav Manik (Ed.), pp. 393-403, Springer Singapore.
2. Sunil D. Kahar, (2017). *Duplex Stainless Steels-An overview*, Int. Journal of Engineering Research and Application, **7**(4), pp. 27-36.
3. Guocai Chai and Pasi kangas, (2016). *Super and hyper duplex stainless steels: structures, proper-ties and applications*, 21st European Conference on Fracture, pp. 1755–1762, Catania, Italy.
4. Erik B. Haugan, Monika Næss, Cristian Torres Rodriguez, Roy Johnsen, and Mariano Ian-nuzzi, (2017). *Effect of Tungsten on the Pitting and Crevice Corrosion Resistance of Type 25 Cr Super Duplex Stainless Steels*, Corrosion, **73**(1), pp. 53-67.
5. Jagesvar Verma, Ravindra Vasantrao Taiwade, (2017). *Effect of welding processes and conditions on the microstructure, mechanical properties and corrosion resistance of duplex stainless-steel weldments*, Journal of Manufacturing Processes, **25**, pp. 134-152.
6. Kai Qi, Ruifeng Li, Guangjin Wang, Gangzhi Li, Bin Liu, and Mingfang Wu, (2019). *Microstruc-ture and Corrosion Properties of Laser-Welded SAF 2507 Super Duplex Stainless Steel Joints*, Journal of Materials Engineering and Performance, **28**, pp. 287–295.
7. Ze-hua Zhu, Wei-dong Zhang, Xiao-hui Tu, Xiao-jian Wang and Wei Li, (2018). *Effect of sigma phase precipitation on microstructure and properties of cast ZG0Cr26Ni5Mo3Cu3 duplex stainless steel under different heat treatments*, China Foundry Research & Development, **15**(3), pp.182-188.
8. Ziying Zhang, Huizhen Zhang, Jun Hu, Xiaoxiao Qi, Yang Bian, Ao Shen, Ping ping Xu, Yiangqiang Zhao, (2018). *Microstructure evolution and mechanical properties of briefly heat-treated SAF2507 super duplex stainless steel welds*, Construction and Building Materials, **168**, pp.338-345.
9. Yu Hu, Yonghua Shi, Xiaoqin Shen, and Zhongmin Wang, (2018). *Microstructure Evolution and Selective Corrosion Resistance in Underwater Multi-pass 2101 Duplex Stainless Steel Welding Joints*, Metallurgical and Materials Transactions A, **49**(8), pp. 3306-3320.
10. N. Sivagurumanikandan, S. Saravanan, G. Shanthos Kumar, S. Rajua, K. Raghukandan, (2018). *Prediction and optimization of process parameters to enhance the tensile strength of Nd YAG laser welded super duplex stainless steel*, Optik, **157**, pp.833-840.
11. Suryana, Agus Pramono, Iskandar Muda, and Ade Setiawan, (2019). *The Influence of Heat Input to Mechanical Properties and Microstructures of API 5L-X65 Steel Using Submerged Arc Welding Process*, MATEC Web of Conferences, IIW 2018, **269**, 01009.
12. S. Saravanana, N. Sivagurumanikandan, K. Raghukandan, (2019). *Effect of heat input on micro-structure and mechanical properties of Nd YAG laser welded super duplex stainless steel-numerical and experimental approach*, Optik, **185**, pp.447-455.
13. W. W. Zhang, S. Cong, S. B. Luo, and J. H. Fang, (2018). *Effects of Energy Density and Shielding Medium on Performance of Laser Beam Welding (LBW) Joints on SAF2205 Duplex Stain-less Steel*, JOM, **70**(8), pp.1554-1559.
14. Hsieh, RI., Liou, HY. & Pan, YT. (2001). *Effects of cooling time and alloying elements on the microstructure of the gleeble-simulated heat-affected zone of 22% Cr duplex stainless steels*. J. of Materi Eng and Perform 10, pp. 526–536.
15. L Karlsson, L Ryen, S Pak, (1995). *Precipitation of intermetallic phases in 22% Cr duplex stainless weld metals*, Welding Journal, **74**(1), pp. 28-38.
16. Tianqi Li, Yingying Zhang, Lei Gao, Yunhao Zhang, (2018). *Optimization of FCAW Parameters for Ferrite Content in 2205 DSS Welds Based on the Taguchi Design Method*. Hindawi, Advances in Materials Science and Engineering, **7**, pp.1-7.
17. G Bansal Rajkumar, N Murugan, (2014). *Development of Regression Models and Optimization of FCAW Process Parameter of 2205 Duplex Stainless Steel*. Indian Journal of Engineering & Materials Science, **21**, pp. 149-154.
18. Koray Yurtisik, Suha Tirkes, Igor Dykhno, C. Hakan Gur, Riza Gurbuz, (2013). *Characterization of Duplex Stainless-Steel Weld Metals Obtained by Hybrid Plasma-Gas Metal Arc Welding*, Soldag. Insp. So Paulo, **18**(3), pp. 207-216.
19. Burcu Tolunguc, (2012). *Microstructural and Mechanical Characterization of duplex Stainless-Steel Grade 2205 Joined by Hybrid Plasma and Gas Metal Arc Welding*, Master's Thesis, Middle East Technical University.
20. Kadivendi Srinivas, Pandu R. Vundavilli, M. Manzoor Hussain, (2018). *Optimization of Weld Bead Parameters of Plasma Arc Welding Using GA and IWO*. S. S. Hiremathetal. (eds.), Select Proceedings of ICAMT 2018, LNCS, pp. 17–24. Springer.
21. M. A. Daha, G. A. Nassef, I. A. Abdallah, H. M. Abouseeda, (2012). *Three-Dimensional Thermal Finite Element Modeling for Keyhole Plasma Arc Welding of 2205 Duplex Stainless Steel Plates*, International Journal of Engineering and Technology, **2**(4), pp.720-728.
22. Shane Fatima, Mushtaq Khan, Syed Husain Imran Jaffery, Liaqat Ali, Mohammad Mujahid and Shahid I Butt, (2015). *Optimization of Process Parameters for Plasma Arc Welding of Austen-itic Stainless Steel (304 L) With Low Carbon Steel (A-36)*, Proc Imeche Part L: J Materials: Design and Applications., pp. 1-14.
23. Tushar Ramdas Dandekar, Aman Gupta, Amit Kumar, Rajesh Kisni Khatirkar, (2018). *Basavaraj*

Vadavadagi, Shielded metal arc welding of UNS S32750 steel: microstructure, mechanical properties and corrosion behavior, Research Materials Express, **5**(10), 106506.
24. Aman Gupta, Amit Kumar, T. Baskaran, Shashi Bhushan Arya, Rajesh Kisni Khatirkar, (2018). *Effect of Heat Input on Microstructure and Corrosion Behavior of Duplex Stainless-Steel Shielded Metal Arc Welds*, Transactions of the Indian Institute of Metals, **71**(7), pp.1595-1606.
25. Suryana, Agus Pramono, Iskandar Muda and Ade Setiawan, *The Influence of Heat Input to Mechanical Properties and Microstructures of API 5L-X65 Steel Using Submerged Arc Welding Process*, MATEC Web of Conferences, IIW 2018, **269**, 01009.
26. Kondapalli Siva Prasad, Ch. Srinivasa Rao, D. Nageswara Rao, (2012) *Effect of pulsed current micro plasma arc welding process parameters on fusion zone grain size and ultimate tensile strength of Inconel 625 sheets*, Acta Metallurgica Sinica (English letters), **25**, pp.179-189.
27. Kondapalli Siva Prasad, Ch. Srinivasa Rao, D. Nageswara Rao, (2015). *Optimization of fusion zone grain size, hardness and ultimate tensile strength of pulsed current micro plasma arc welded Inconel 625 sheets using genetic algorithm*, International Journal of Advanced Manufacturing Technology (Springer), **85**(8-12), pp.2287-2295.

8. ACKNOWLDGEMENTS

The authors would like to thank Aesteiron steels, Mumbai for supplying the material and the micro plasma arc welding facility was provided by Metallic Bellows (I) Pvt. Ltd. in Chennai, India.

Received: February 26, 2022 / Accepted: June 15, 2022 / Paper available online: June 20, 2022 © International Journal of Modern Manufacturing Technologies